Ocean Engineering 362 (2026) 126189

Contents lists available at ScienceDirect

Ocean Engineering

journal homepage: www.elsevier.com/locate/oceaneng

Research paper

# Wave-induced effects on tidal turbine performance and structural loading: A CFD study across varying submergence depths

Kangmin Kim [a], Gyeongseo Min [a], Haechan Yun [a], Younguk Do [a], KeoungHyun Jung [a], Weichao Shi [b,*], Daejeong Kim [c,**], Soonseok Song [a,***]

[a] Department of Naval Architecture & Ocean Engineering, Inha University, South Korea
[b] School of Engineering, Newcastle University, United Kingdom
[c] Division of Navigation Convergence Studies, Korea Maritime & Ocean University, South Korea

ARTICLE INFO

*Keywords:*
Tidal turbine
Ocean waves
Copper loss
Torque fluctuation
Computational fluid dynamics (CFD)

ABSTRACT

Tidal energy offers significant potential as a predictable renewable resource; however, given that ocean waves introduce complex flow oscillations, incorporating wave-induced effects into the design process is essential for ensuring both performance and structural durability. This study evaluates the hydrodynamic response of a tidal turbine across various submergence depths under representative wave conditions using Computational Fluid Dynamics (CFD). The research quantifies the impact of wave-current interaction on both overall performance and individual blade loading. The study employs the Unsteady Reynolds-Averaged Navier–Stokes (URANS) approach, analysing four hub submergence depths (0.5D, 1.0D, 1.5D, and 2.0D) under wave conditions. The analysis focuses on the cyclic fluctuations of thrust, torque, and power, and explains the resulting effects on generator copper losses. Additionally, particular emphasis is placed on the unsteady loads acting on the blades as they rotate through the wave-induced velocity field. The numerical results indicate that torque fluctuates from +91% to −68% relative to the mean, which increases generator copper losses and reduces power conversion efficiency.

## 1. Introduction

Global warming and the resulting climate change have significantly increased worldwide demand for sustainable and low-carbon energy sources. Consequently, renewable energy technologies have attracted attention as viable alternatives to fossil fuels. Tidal and ocean current energy are recognized as highly promising energy sources due to their exceptional predictability and high energy density compared to other renewable energy types. Beyond their reliability, these resources offer the advantage of minimal visual impact and high power-generation consistency, as they are independent of fluctuating weather conditions like solar or wind energy sources. Based on these characteristics, several commercial-scale applications in actual sea areas have been demonstrated, such as the MeyGen 1.5 MW horizontal axis tidal turbine and Orbital Marine Power's O2 rated 2 MW tidal turbine (MeyGen Ltd, 2019; Orbital Marine Power, 2022). However, despite this progress, much of the foundational research has been conducted under highly controlled laboratory settings or idealised steady-flow conditions. In practice, tidal turbines must operate within the complex, dynamic environment of the upper water column, where they are continuously exposed to ocean waves. Therefore, bridging the gap between controlled environment studies and real-world operational scenarios is essential for the successful commercialisation of tidal energy.

Research to investigate the hydrodynamic performance of tidal turbines has been primarily conducted through experimental approaches in the early stages (Bahaj et al., 2007a, 2007b). presented experimental reference data for tidal turbine performance evaluation. Subsequently, Blade Element Momentum Theory (BEMT) has been widely utilized as a theoretical approach to efficiently predict tidal turbine performance. BEMT has been applied as a suitable method for preliminary design and performance analysis of tidal turbines due to its high computational efficiency. Many BEMT-based performance prediction models for tidal turbines have been developed, and the validity of performance predictions has been verified by comparing them with experimental results. Additionally, BEMT models that consider Reynolds number effects when extrapolating experimental-scale results to full-scale have been

* Corresponding author.
** Corresponding author.
*** Corresponding author.
*E-mail addresses:* weichao.shi@newcastle.ac.uk (W. Shi), kdj4907@kmou.ac.kr (D. Kim), s.song@inha.ac.kr (S. Song).

https://doi.org/10.1016/j.oceaneng.2026.126189
Received 27 February 2026; Received in revised form 17 April 2026; Accepted 20 May 2026
Available online 27 May 2026

developed (e.g., Allsop et al., 2017; Batten et al., 2008; Masters et al., 2011). Computational Fluid Dynamics (CFD) is another method for evaluating tidal turbine performance. CFD is characterized by its ability to directly analyse the flow field around tidal turbines and the hydrodynamic forces acting on blades, enabling analysis not only of average performance but also of unsteady loads, wake structures, and detailed flow. Ahmed et al. (2017) performed CFD analysis and verified the reliability of CFD-based performance prediction by comparing it with measured data. Apsley et al. (2018) analysed thrust, power, and flapwise bending moment of tidal turbines in close arrays using RANS-based CFD and quantitatively analysed wake interaction effects. Min et al. (2025) analysed performance changes of tidal turbines under free surface exposure conditions using CFD and quantitatively evaluated power reduction under partially submerged conditions.

Thus, the understanding of tidal turbine performance has gradually deepened as research approaches have expanded from experimental studies to BEMT, BEM-CFD coupled models, and CFD analysis.

However, the performance of tidal turbines can vary significantly depending on environmental conditions such as waves and wind. Waves induce periodic orbital motion of water particles, changing horizontal and vertical velocities, which causes tidal turbines to experience a complex velocity field different from that in still water. In this context, numerous studies have been conducted on tidal turbine behaviour under wave conditions. El-Shahat et al. (2021) analysed wave-current interaction of tidal turbines by combining BEMT and wave theory, quantitatively evaluating the range of periodic fluctuations in unsteady thrust and torque. Gaurier et al. (2013) analysed that in the presence of waves, the instantaneous angle of attack of blades, pressure distribution around blades, and effective inflow velocity of the rotor are affected by wave-induced velocities and orbital motion. Si et al. (2024) explained that load fluctuations are significantly amplified at specific frequency components due to nonlinear interaction between wave-induced velocities and rotor rotation, and that these effects are further strengthened with increasing wave period and height. Examining research results on the effect of waves on turbine average performance, Martinez et al. (2018) found that average applied loads increase by 5% in the presence of waves. Perez et al. (2022) reported that long-period waves can double the average performance coefficient, and Guy et al. (2024) reported that in the presence of waves, the time-averaged torque of the turbine increases by 22% and thrust by 11%. The differences in these research results are attributed to the fact that, as presented by Si et al. (2024), the tendency of the effect on turbine performance varies greatly depending on wave period and height.

While these CFD-based studies have significantly advanced our capability to predict turbine responses, there remains an opportunity to further explore the high-fidelity interaction between the free surface and the rotor under wave condition. Much of the existing numerical literature has focused on fixed installation depths or isolated wave conditions. However, the capacity of CFD to resolve complex free-surface interfaces and calculate unsteady loads on individual blades allows for a more nuanced investigation into how wave-induced effects are modulated by varying submergence depths. Considering that a turbine's operating depth relative to the free surface fluctuates with the tidal range in actual sea states, a systematic analysis of these effects is essential for refining operational reliability.

To address this specific area, the present study employs the CFD simulations to quantify torque variability and evaluate the influence of varying submergence depths on tidal turbine performance. By building upon the established numerical frameworks, this research aims to provide a comprehensive assessment of the structural implications arising from unsteady loads in combined wave-current environments.

## 2. Methodology

### 2.1. Governing equation

In this study, a computational fluid dynamics (CFD) model for assessing wave-induced effects on tidal turbines is developed using the commercial software package STAR-CCM+ (version 19.04.009). The numerical framework employs the Unsteady Reynolds–Averaged Navier–Stokes (URANS) approach to solve the governing equations for incompressible turbulent flows. The continuity and momentum equations are expressed in tensor notation using Cartesian coordinates as follows:

Continuity equation:

$$\frac{\partial \rho}{\partial t} + \frac{\partial (\rho u_i)}{\partial x_i} = 0 \tag{1}$$

Momentum equation:

$$\frac{\partial (\rho u_i)}{\partial t} + \frac{\partial}{\partial x_j}\left(\rho u_i u_j + \rho u_i' u_j'\right) = -\frac{\partial \overline{p}}{\partial x_i} + \frac{\partial \tau_{ij}}{\partial x_j} \tag{2}$$

where $\rho$ denotes the fluid density, $u_i$ represents the time-averaged velocity components, $u_i' u_j'$ is the Reynolds stress tensor, $\overline{p}$ is the mean pressure, and $\tau_{ij}$ represents the viscous stress tensor components. For a Newtonian fluid, the viscous stress tensor is expressed as:

$$\tau_{ij} = \mu\left(\frac{\partial u_i}{\partial x_j} + \frac{\partial u_j}{\partial x_i}\right) \tag{3}$$

where $\mu$ is the dynamic viscosity of the fluid.

The Reynolds stresses arising from turbulent fluctuations in Eq. (2) require appropriate closure modeling. The Boussinesq eddy viscosity hypothesis is employed to relate the Reynolds stresses to the mean velocity gradients:

$$-\rho u_i' u_j' = \mu_t\left(\frac{\partial u_i}{\partial x_j} + \frac{\partial u_j}{\partial x_i}\right) - \frac{2}{3}\rho k \delta_{ij} \tag{4}$$

where $\mu_t$ is the turbulent eddy viscosity, k is the turbulent kinetic energy, and $\delta_{ij}$ is the Kronecker delta.

The computational domain was discretized using the Finite Volume Method (FVM), which subdivides the solution domain into a finite number of contiguous control volumes. The governing equations were converted into algebraic equations and solved numerically through a control-volume-based technique. The FVM is particularly suitable for complex geometries due to its capability to accommodate arbitrary grid topologies. The Semi-Implicit Method for Pressure-Linked Equations (SIMPLE) algorithm was employed for pressure-velocity coupling, adopting a predictor-corrector approach to link the continuity and momentum equations. The momentum equations were discretized using second-order convection schemes, while second-order temporal discretization was applied throughout the simulations to ensure temporal accuracy.

For turbulence modelling, the Shear Stress Transport (SST) k–ω model was adopted. This model effectively blends the k–ω formulation in the near-wall region with the k–ε model in the free-stream, providing enhanced predictive capability in adverse pressure gradients and flow separation regions. The SST k–ω model has been extensively validated for marine turbine applications and offers superior performance in capturing complex flow phenomena around rotating blades. An all–$y^+$ wall treatment was implemented, maintaining $y^+$ values appropriate for accurate turbulent boundary layer resolution.

The free surface was captured using the Volume of Fluid (VOF) multiphase method, which tracks the water-air interface. To enhance interface sharpness and minimize numerical diffusion, the High-Resolution Interface Capturing (HRIC) scheme was employed. Fifth-order Stokes wave theory was implemented to generate realistic wave conditions. This higher-order formulation more accurately represents the nonlinear characteristics of finite-amplitude waves compared to linear wave theory, including the asymmetric wave profile with steeper crests and flatter troughs commonly observed in actual ocean waves.

### *2.2. Geometry and wave conditions*

The present study employed a full-scale horizontal axis tidal turbine (HATT), as illustrated in Fig. 1, to evaluate wave-induced effects under varying submergence conditions (see Fig. 2). This turbine geometry was selected based on its experimental validation in previous studies (Shi et al., 2016), enabling direct comparison between CFD predictions and measured data. The principal dimensions and geometric characteristics of the HATT are summarised in Table 1.

The inflow velocity was set to 3.2 m/s. All simulations were conducted at a tip speed ratio (TSR) of 4, which falls within the range of optimal power extraction efficiency for this turbine configuration. The TSR is defined as:

$$TSR = \frac{\omega r}{V_{in}} \tag{5}$$

where $\omega$ denotes the rotational speed of the turbine (rad/s), $r$ denotes the blade radius (m), and $V_{\text{in}}$ denotes the inflow velocity (m/s).

In actual ocean environments, waves exhibit irregular spectral characteristics. However, since the primary objective of this study is to systematically quantify the effects of waves on tidal turbine performance across varying submergence depths, regular wave conditions were adopted so that the wave parameters could be held constant throughout the simulations. This approach enables the wave-induced effects to be independently isolated and evaluated as a function of submergence depth. The fifth-order Stokes wave theory (Fenton, 1985) was employed for wave generation. This higher-order formulation more accurately reproduces the nonlinear characteristics of finite-amplitude waves, characterised by steeper crests and flatter troughs, compared to linear wave theory. As such, it provides a more physically representative description of the wave conditions considered in this study (El-Shahat et al., 2021). The wave height was set to 4 m, which is consistent with significant wave heights typically observed at tidal energy sites (Lewis et al., 2014). The wave period was specifically chosen, using the TSR definition Eq. (5), to induce resonance with the rotational period of the turbine at TSR 4. This configuration represents a critical loading scenario where wave-induced velocity fluctuations are most likely to amplify unsteady forces on the rotor. The wave parameters employed in this study are presented in Table 2.

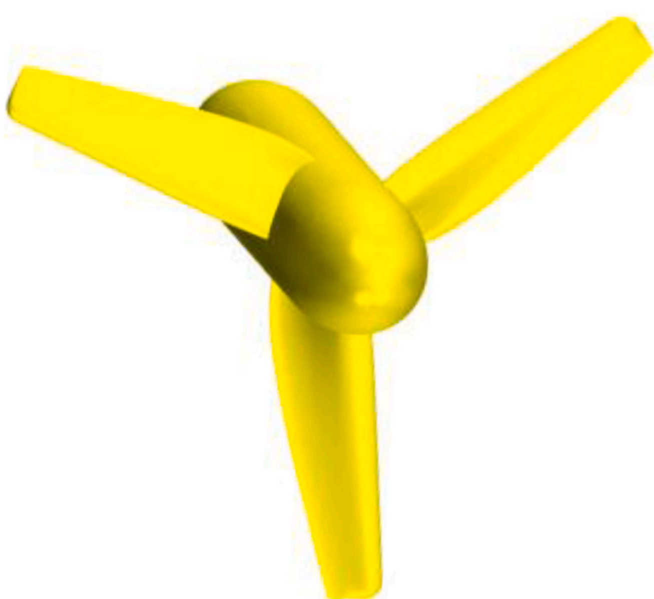

**Fig. 1.** Geometry of the horizontal-axis tidal turbine.

Turbine performance was evaluated using two primary non-dimensional coefficients: the thrust coefficient ($C_T$) and the power coefficient ($C_P$). These coefficients are defined as:

$$C_T = \frac{T}{0.5\rho A_T V_{in}^2} \tag{6}$$

$$C_P = \frac{2\pi n Q}{0.5\rho A_T V_{in}^3} \tag{7}$$

where $T$ denotes the thrust (N), $Q$ denotes the torque (N-m), $\rho$ is the fluid density (kg/m$^3$), $A_T$ denotes the swept area of the rotor (m$^2$), and $V_{\text{in}}$ denotes the inflow velocity (m/s). The thrust and power coefficients are used to evaluate the axial structural loading and power performance of the turbine under wave-influenced operating conditions.

### *2.3. Submergence depth cases*

The primary objective of this study is to quantify how wave-induced hydrodynamic effects vary with turbine submergence depth. To systematically investigate this relationship, simulations were conducted at four different submergence depths under wave conditions, in addition to a baseline calm water case for reference. All simulations were performed at TSR 4, corresponding to near-optimal operating conditions for this turbine configuration.

Four wave cases were defined with submergence depths of 0.5D, 1.0D, 1.5D and 2.0D (where D = 20 m is the rotor diameter), where 0.5D represents shallow, 1.0D and 1.5D represent moderate, and 2.0D represents deep submergence conditions. An additional calm water simulation at 2.0D submergence depth was conducted to isolate wave-induced effects from depth-dependent hydrodynamic characteristics. The complete simulation matrix is summarised in Table 3.

This systematic variation in submergence depth enables a comprehensive evaluation of how the vertical position of the rotor within the water column modulates wave-induced loading and performance variations. This thereby addresses the research gap identified in the literature regarding dynamic submergence effects in tidal energy applications.

### *2.4. Computational domain and boundary conditions*

The computational domain and boundary conditions employed in this study are illustrated in Fig. 3. The domain configuration was designed to accurately capture wave propagation, turbine-induced flow disturbances, and free surface dynamics while minimising computational cost through optimised domain sizing.

#### *2.4.1. Full - scale wave simulations*

For full-scale simulations incorporating wave effects, velocity inlet boundary conditions were applied to all external faces except the top boundary, which was set as a pressure outlet. The rotating region surrounding the turbine was prescribed a rigid-body rotation at the rotational speed corresponding to TSR 4. This approach, utilising the Sliding Mesh technique, enables accurate resolution of unsteady blade forces and wake development in the presence of free surface motion.

In contrast, simulations without free surface effects (i.e., fully submerged conditions for validation purposes) were performed using the Multiple Reference Frame (MRF) approach. This steady-state approximation method eliminates the need for physical mesh motion whilst maintaining the relative velocity gradients between the rotating and stationary regions. The MRF method was specifically employed for validation against model-scale experimental data, where free surface effects were absent due to the cavitation tunnel testing environment.

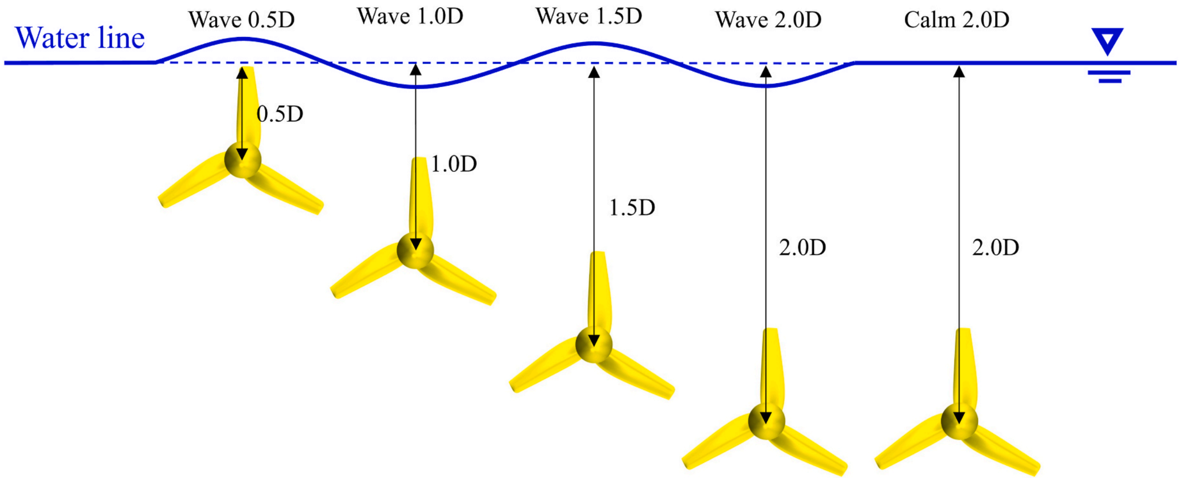


**Fig. 2.** Simulation cases: turbine positions at different submergence depths (0.5D, 1.0D, 1.5D, 2.0D) under wave conditions.

**Table 1**
Specifications of the horizontal-axis tidal turbine.

| Main Dimension of HATT | |
|---|---|
| Diameter (m) | 20 |
| Number of blades | 3 |
| Airfoil | S814 |

**Table 2**
Wave and current parameters used in the CFD simulations.

| Parameter | Value |
|---|---|
| Wave Model | Fifth Order Stokes Wave |
| Current Speed (m/s) | 3.2 |
| Wave Height (m) | 4 |
| Wave Period (s) | 4.91 |

**Table 3**
Simulation cases and operating conditions.

| Case ID | Wave 0.5D | Wave 1.0D | Wave 1.5D | Wave 2.0D | Calm 2.0D |
|---|---|---|---|---|---|
| Submergence Depth | 0.5D | 1.0D | 1.5D | 2.0D | 2.0D |
| Condition | Wave | Wave | Wave | Wave | Calm Sea |
| TSR | 4 | 4 | 4 | 4 | 4 |

### 2.4.2. *Wave generation and absorption*

In accordance with ITTC (2011) guidelines, the computational domain boundaries were positioned at sufficient distances from the turbine to minimize their influence on the flow solution. For wave condition simulations, forcing zones were implemented at these four domain boundaries, as illustrated in Fig. 4. As noted by Ferziger et al. (2002), the velocity components and volume fraction of water within the forcing zone are progressively driven toward the analytical solution of fifth-order Stokes wave theory (Fenton, 1985). Consequently, turbine-induced disturbances to the incoming wave field are gradually dissipated within the forcing zone, thereby preventing spurious wave reflections at the domain boundaries.

## 2.5. *Mesh generation*

The computational grid system was generated using the automatic meshing facility in STAR-CCM+ (version 19.04.009), which

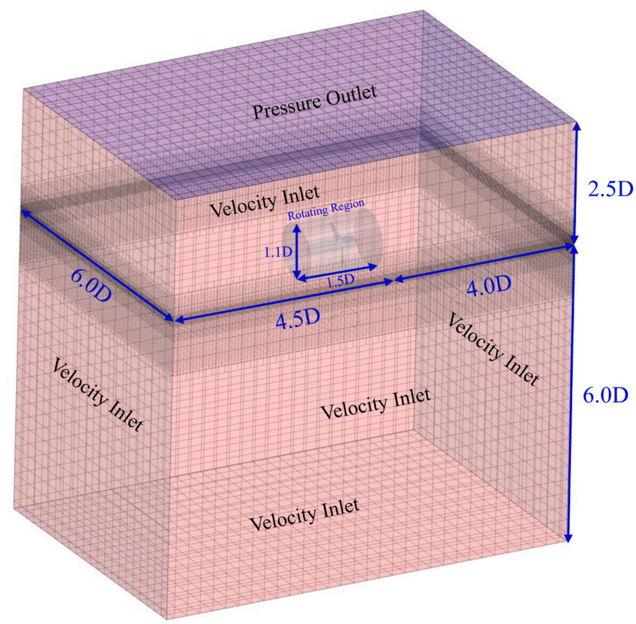


**Fig. 3.** Computational domain and boundary conditions used in the CFD simulations.

automatically creates surface and volume grids suitable for the finite volume method. A surface remesher tool was employed to enhance the overall quality of geometric surfaces and optimise mesh quality for the volume grids. A trimmed cell mesher was utilized for volume mesh generation. The prism layer mesh model was adopted to provide orthogonal prismatic cells near wall surfaces and boundaries, which was essential for accurate resolution of near-wall flow characteristics.

Local mesh refinements were strategically applied in critical flow regions to capture both wave dynamics and turbine-induced flow structures. Following the guidelines established by ITTC (2011) for wave simulations, the free surface region was refined with a minimum of 80 cells per wavelength in the horizontal direction and 20 cells per wave height in the vertical direction. This refinement density ensured adequate resolution of wave profiles and prevented numerical diffusion from distorting the free surface shape during wave propagation.

The thickness of the first prism layer cell adjacent to the blade surface was carefully selected to maintain wall $y^+$ values greater than 30 for all blade and hub surfaces, which was appropriate for full-scale Reynolds numbers when employing wall functions with the SST $k$-$\omega$ turbulence

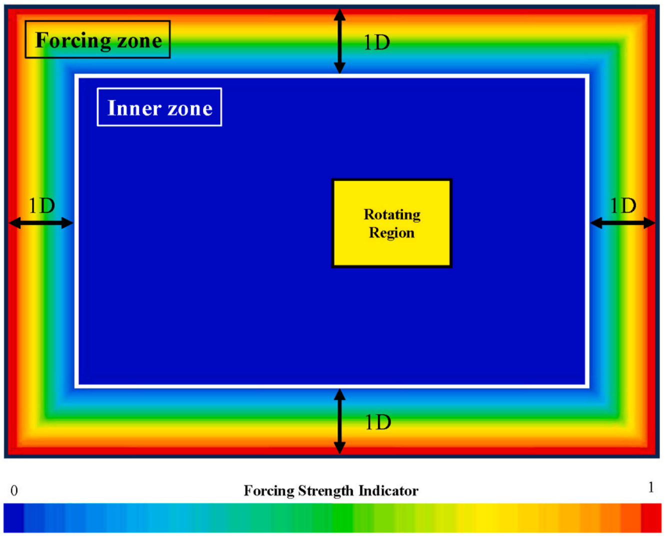


**Fig. 4.** Forcing zones used in the CFD simulations.

model. As illustrated in Fig. 5, the free surface refinement zone exhibited a wider spatial extent compared to typical wake refinement regions, to account for the lateral spread of wave-induced velocity fluctuations and turbine-generated surface disturbances. This broader refinement strategy ensured that wave propagation characteristics remained unaffected by numerical dissipation throughout the computational domain.

## 3. Validation and verification

### 3.1. Validation study

The CFD model was validated against experimental measurements obtained from the cavitation tunnel tests reported by Shi et al. (2016), and the validation simulations were performed at the scale of the cavitation tunnel. Model-scale simulations were performed using the MRF approach under identical geometric and flow conditions as the experiments, with the turbine operating at TSR values ranging from 3 to 6. Fig. 6 presents a comparison of the predicted thrust coefficient ($C_T$) and power coefficient ($C_P$) against the experimental data across this TSR range.

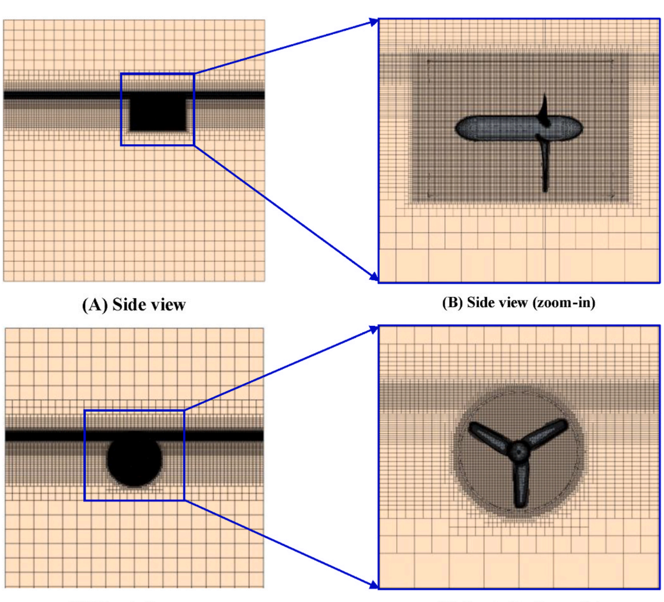


**Fig. 5.** Volume mesh.

As shown in Fig. 6, the CFD predictions exhibit good agreement with experimental measurements throughout the operational range. The discrepancies between the experimental data and CFD results were within an acceptable ranges for RANS-based turbulence modelling, where uncertainties in turbulence closure and wall treatment could introduce variations of this order.

### 3.2. Verification study

The verification study focused on the Wave 2.0 $D$ submergence case to estimate numerical uncertainties associated with spatial and temporal discretization. Following the Grid Convergence Index (GCI) method developed by Celik et al. (2008), systematic refinement studies were conducted at TSR 4 to assess the reliability of the computational results.

Three progressively refined grid levels were generated by systematically reducing the base cell size whilst maintaining a constant refinement ratio between successive meshes. In addition, three time step levels were examined to evaluate temporal convergence behaviour. The uncertainty analysis demonstrated that both the thrust coefficient and power coefficient exhibited grid uncertainties of less than 1%, indicating reliable numerical predictions. Based on these convergence studies, a time step of 0.01 s and the medium mesh were selected for all subsequent simulations. This time step satisfies the ITTC (2011) recommendation that the time interval should be smaller than the time required for the turbine to rotate 2°. The complete convergence test results are presented in Tables 4 and 5.

## 4. Results

### 4.1. Influence of submergence depth on wave-induced effects

Figs. 7 and 8 present the instantaneous velocity field and dynamic pressure distribution around the tidal turbine for all five simulation cases. These visualisations provide a qualitative illustration of the fundamental differences in the flow environment experienced by the turbine under calm water and wave conditions.

Under calm water conditions (Calm 2.0D), the velocity field is characterised by a symmetric and stable wake structure downstream of the rotor, with no significant disturbance near the free surface. The dynamic pressure distribution similarly remains uniform and steady, reflecting the absence of wave-induced perturbations.

In contrast, all wave cases exhibit markedly different flow fields. The interaction between the wave-induced orbital velocities and the rotor inflow introduces periodic disturbances in both the velocity and dynamic pressure fields, with the intensity of these disturbances increasing progressively as the submergence depth decreases. In the Wave 0.5D case, the influence of the free surface is most pronounced, with the velocity and dynamic pressure fields showing strong asymmetry and large spatial gradients near the rotor plane. The intermittent exposure of the blade tips to air during wave troughs further disrupts the flow field, resulting in an abrupt transition between the water and air phases that is clearly visible in both figures. At deeper submergence depths (Wave 1.5D and Wave 2.0D), the wave-induced disturbances are progressively attenuated, and the flow fields more closely resemble those observed under calm water conditions, consistent with the exponential decay of wave orbital velocities with depth.

Figs. 7 and 8 visually demonstrate that the wave-induced velocity field is the underlying cause of the increased oscillations in torque and blade loading presented in Figs. 9–13. These qualitative observations are consistent with the quantitative results presented in the following sections and collectively demonstrate that wave conditions fundamentally alter the hydrodynamic environment experienced by the turbine, with direct implications for both performance variability and structural loading.

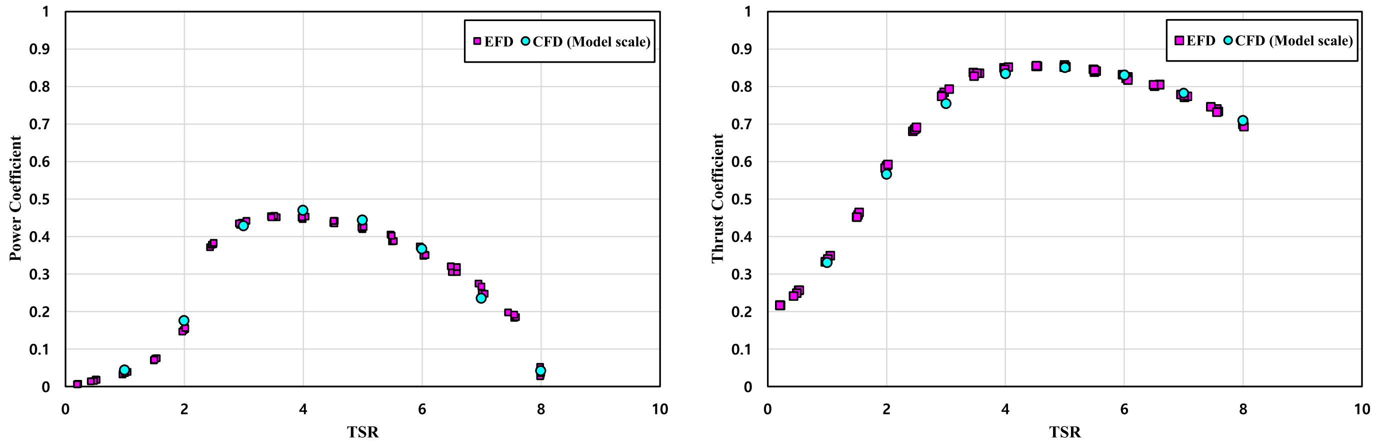


**Fig. 6.** Validation of CFD results: comparison of thrust coefficient ($C_T$) and power coefficient ($C_P$) with experimental data.

**Table 4**
Convergence test for Thrust coefficient.

| | | | | | |
|---|---|---|---|---|---|
| Spatial convergence test | | No. Cells | $C_T$ | | |
| | Coarse | 2,856,335 | 0.8564 | | |
| | Medium | 3,874,629 | 0.8575 | | |
| | Fine | 5,310,658 | 0.8588 | | |
| | | | | $U_{Grid}$ (Mid) | 0.15% |
| Temporal convergence test | | Time step | $C_T$ | | |
| | Coarse | 0.02 | 0.8656 | | |
| | Medium | 0.01 | 0.8575 | | |
| | Fine | 0.005 | 0.8533 | | |
| | | | | $U_{Grid}$ (Mid) | 0.28% |
| | Total uncertainty | | | $U_{total}$ | 0.32% |

**Table 5**
Convergence test for power coefficient.

| | | | | | |
|---|---|---|---|---|---|
| Spatial convergence test | | No. Cells | $C_p$ | | |
| | Coarse | 2,856,335 | 0.4704 | | |
| | Medium | 3,874,629 | 0.4720 | | |
| | Fine | 5,310,658 | 0.4735 | | |
| | | | | $U_{Grid}$ (Mid) | 0.26% |
| Temporal convergence test | | Time step | $C_p$ | | |
| | Coarse | 0.02 | 0.4797 | | |
| | Medium | 0.01 | 0.4720 | | |
| | Fine | 0.005 | 0.4681 | | |
| | | | | $U_{Grid}$ (Mid) | 0.46% |
| | Total Uncertainty | | | $U_{total}$ | 0.53% |

### 4.1.1. *Torque*

Fig. 9(a) presents the torque as a function of normalised time for each submergence depth condition. Data from the initial transient period were excluded from the post-processing, and only the data obtained after the simulation had converged to a periodic steady state were used. The time axis is normalised by the wave period T such that one complete cycle of torque variation is represented. The still-water reference case (Calm 2.0D) exhibits a nearly constant torque with minimal fluctuation, demonstrating the steady-state characteristics of turbine operation under uniform flow conditions. Calm 2.0D provides a well-defined baseline against which wave-induced effects can be quantified.

In contrast, all wave cases exhibit pronounced periodic torque fluctuations, with the amplitude of variation increasing dramatically as submergence depth decreases. At the deepest submergence (Wave 2.0D), torque fluctuations remain relatively moderate, indicating that the rotor operates in a flow regime where wave-induced orbital velocities are largely attenuated with depth. As submergence decreases to 1.5D and 1.0D, the amplitude of torque oscillations progressively intensifies. The shallowest configuration (Wave 0.5D) exhibits extreme torque variability, with oscillations spanning from −68% to +91% of the mean value. These severe fluctuations arise from the combined effects of wave orbital velocities, proximity to the free surface, and the periodic blade exposure during wave troughs.

Fig. 9(b) presents the variation in mean torque and its fluctuation range (min-max) as a function of submergence depth under wave conditions. The standard deviation values for each simulation are illustrated in Fig. 10 and summarised in Table 6. Mean torque increases as the rotor approaches the free surface. This phenomenon can be attributed, following Shi et al. (2016) to the vertical distribution of wave-induced velocities, which are maximised at the free surface and decay exponentially with depth in accordance with wave theory. Consequently, the upper portion of the rotor disk experiences enhanced incident velocity when positioned near the free surface, resulting in elevated mean torque despite the increased unsteadiness.

The Wave 0.5D case exhibits the largest fluctuation range, with a torque variation of approximately 159% between peak and minimum values (−68% to +91% relative to the mean). As submergence depth increases, the fluctuation amplitude decreases exponentially, consistent with the theoretical attenuation of wave-induced velocities with depth. At a submergence of 2.0D, the fluctuation range reduces to approximately ±6%, approaching the steady-state behaviour observed in the still-water case.

### 4.1.2. *Thrust coefficient & power coefficient*

Fig. 11 presents the time-series data of the thrust coefficient ($C_T$) and power coefficient ($C_P$) for each submergence depth condition. As with the torque presented in Fig. 9, the time axis is normalised by the wave period T following the same post-processing procedure described previously. Fig. 12 quantitatively illustrates the influence of submergence depth on the overall performance characteristics of the turbine, displaying the mean thrust and power coefficients alongside their fluctuation ranges as min-max bars.

Both the thrust coefficient and power coefficient exhibit trends consistent with those observed for torque. As submergence depth decreases, the amplitude of fluctuation in both coefficients increases sharply, with the greatest variability observed in the shallowest case

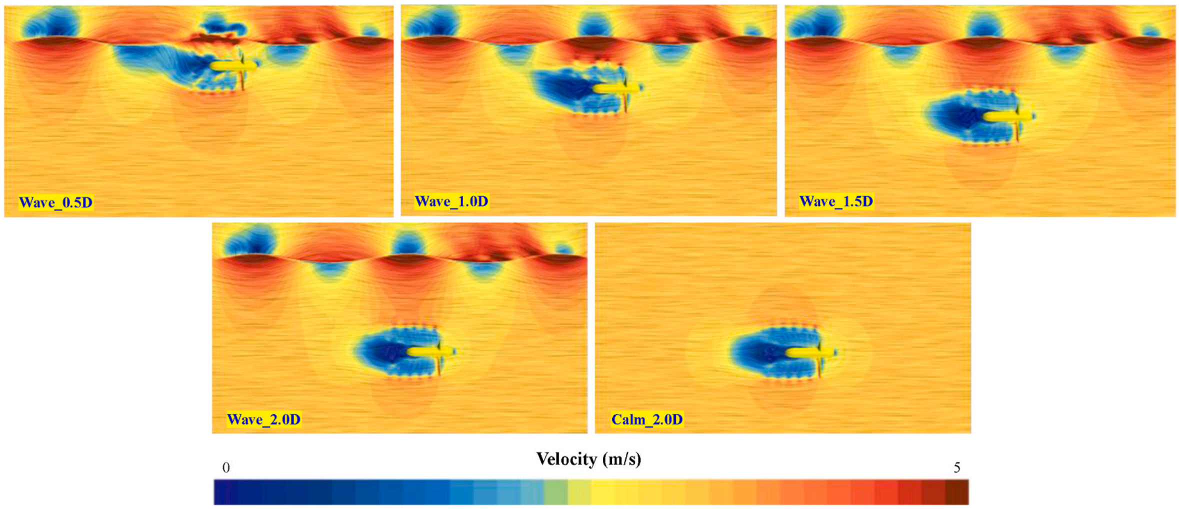


**Fig. 7.** Instantaneous velocity field around the tidal turbine for all five simulation cases.

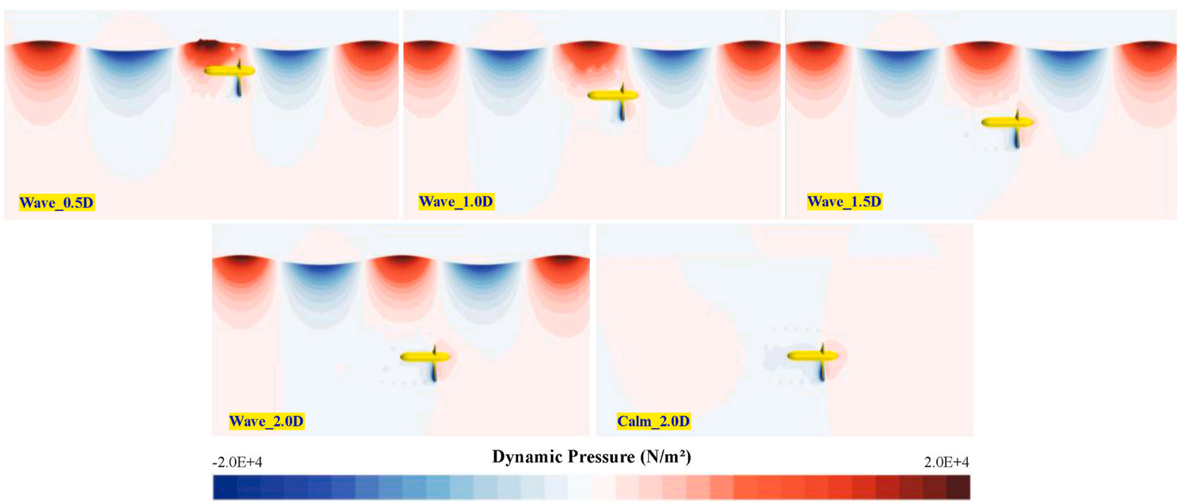


**Fig. 8.** Instantaneous dynamic pressure distribution around the tidal turbine for all five simulation cases.

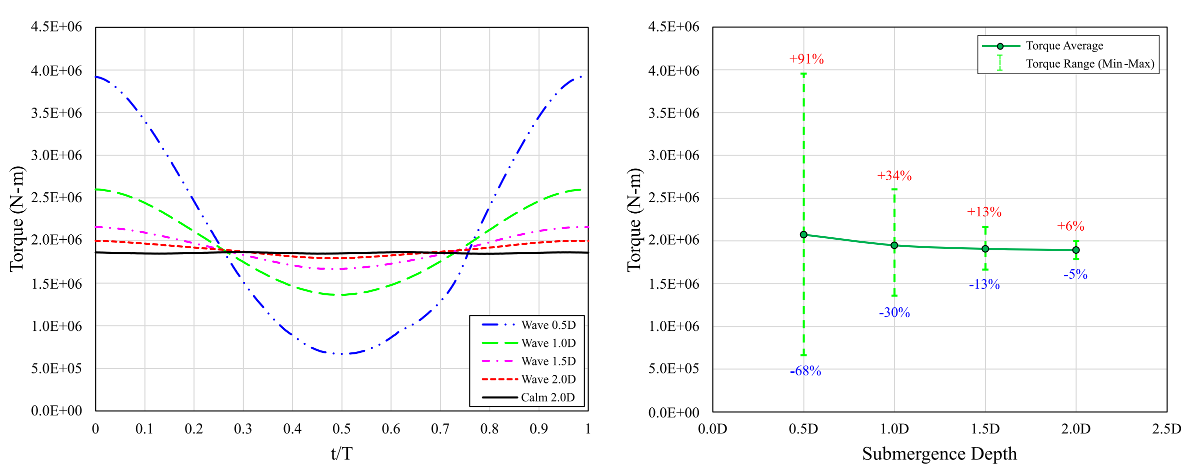


(a) Time series of torque

(b) Mean torque and torque range (Min-Max)

**Fig. 9.** Torque characteristics at different submergence depths: (a) normalised torque over one complete rotation cycle and (b) mean torque with fluctuation range.

(Wave 0.5D). The quantitative results are summarised in Tables 7 and 8, including mean, maximum, minimum, and standard deviation values.

As shown in the tables, the standard deviations of both $C_T$ and $C_P$ increase as the rotor approaches the free surface, consistent with the

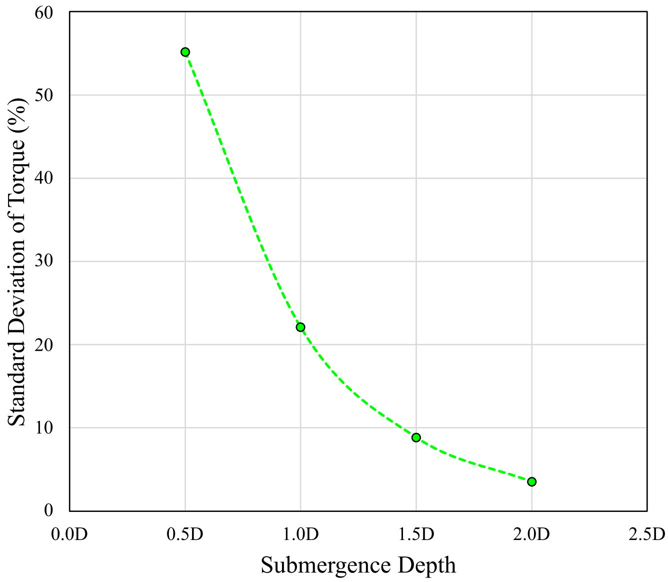


**Fig. 10.** Standard deviation of torque as a function of submergence depth.

trend previously observed for torque. The standard deviation of $C_T$ reaches its maximum of 29.64% at Wave 0.5D and decreases to 1.76% at Wave 2.0D. $C_P$ follows the same pattern, declining from 28.49% to 1.66%.

Regarding mean values, $C_T$ and $C_P$ exhibit different trends. The mean $C_P$ increases progressively as submergence depth decreases, rising from 0.472 at Wave 2.0D to 0.516 at Wave 0.5D. This is attributable to the wave-induced velocities being greatest near the free surface.

The mean $C_T$, by contrast, exhibits non-monotonic behaviour, increasing as the rotor approaches the free surface before declining at the 0.5D case. The Wave 1.0D case yields the highest mean $C_T$ of 0.866, while Wave 0.5D registers a reduced value of 0.854. This is attributed to the intermittent exposure of a portion of the blades to air during wave troughs under Wave 0.5D conditions, which reduces the effective swept area of the rotor.

Examining the fluctuation ranges, the Wave 0.5D case exhibits extreme variability, with $C_T$ spanning from 0.456 to 1.304 and $C_P$ ranging from 0.165 to 0.987. In contrast, the Wave 2.0D case demonstrates stable performance, with $C_T$ confined to the range of 0.830–0.886 and $C_P$ to 0.446–0.499. This highlights that $C_P$ is more sensitive to velocity variations than $C_T$, consistent with the theoretical relationship whereby power scales with the cube of velocity while thrust scales with the square.

The intermediate-depth cases (Wave 1.0D and 1.5D) exhibit characteristics intermediate between the two extremes in terms of both mean performance and variability. This systematic pattern of variation provides a basis for evaluating the trade-off between mean performance and fluctuation amplitude when selecting the installation depth.

### 4.2. Generator efficiency: copper loss analysis

The torque fluctuations induced by wave loading have direct implications for generator performance beyond the hydrodynamic domain. In a permanent magnet synchronous generator (PMSG), the electromagnetic torque is proportional to the stator current, expressed as $T = kI$, where k is the machine constant (Chapman, 2003). Consequently, copper losses, defined as $P_{copper} = I^2R$, scale with the square of the RMS torque, as expressed below:

$$P_{copper} \propto \mathrm{T}_{\mathrm{rms}}^2 = T_{mean}^2 + \sigma^2 \tag{8}$$

This relationship demonstrates that even when the mean torque remains approximately constant, an increase in torque standard deviation $\sigma$ directly elevates the RMS torque and therefore the copper losses in the generator windings.

To quantify this effect, a simplified copper loss analysis is conducted based on the torque time-series data obtained from the CFD simulations. It is assumed that copper loss constitutes the dominant loss mechanism in the generator, and a baseline generator efficiency of $\eta_0 = 0.90$ is assigned to the still-water reference case (Calm 2.0D). The value of $\eta_0 = 0.90$ is adopted as a conservative representative value corresponding to the lower bound of the 90–95% range generally reported for direct-drive PMSG systems, ensuring that the influence of wave-induced torque fluctuations is not underestimated in the present analysis. The copper losses for each wave case are estimated from the RMS torque and scaled relative to the baseline. The generator efficiency is defined as follows:

$$\eta = \frac{P_{output}}{P_{input}} = \frac{P_{input} - P_{copper}}{P_{input}} \tag{9}$$

It must be emphasised that this analysis does not account for iron losses, mechanical losses, or power converter losses. The purpose is not to provide a precise prediction of absolute generator efficiency, but rather to illustrate the trend by which wave-induced torque variability degrades the copper loss performance of the generator.

The results are summarised in Table 9.

The results demonstrate a clear and systematic relationship between

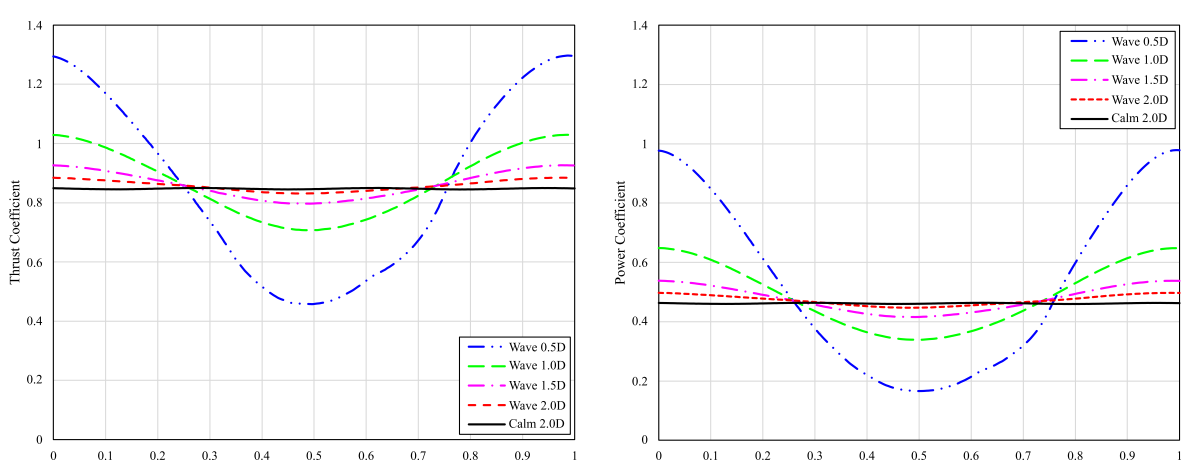


(a) Time series of thrust coefficient

(b) Time series of power coefficient

**Fig. 11.** (a) Thrust coefficient and (b) power coefficient as a function of normalised time (t/T).

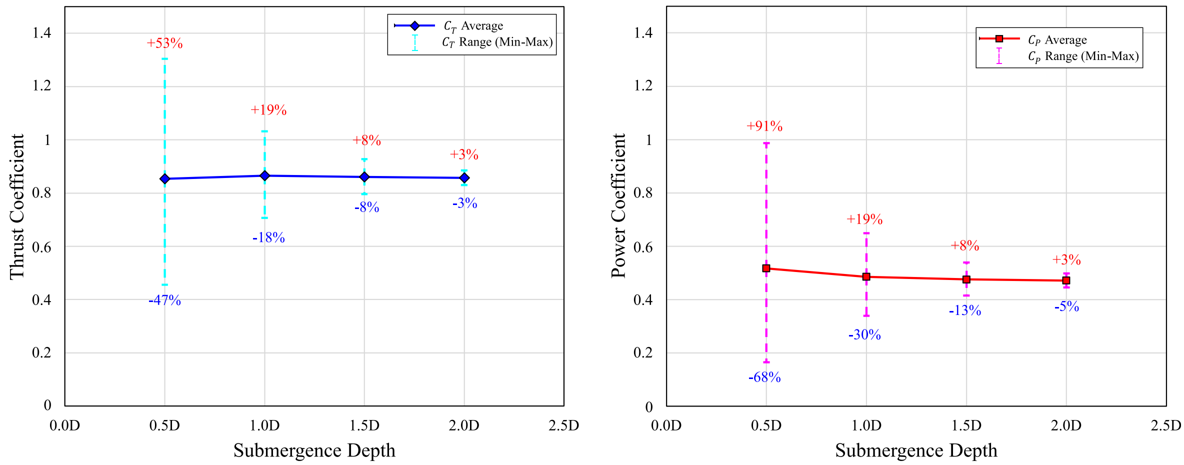


(a) Mean thrust coefficient and thrust coefficient range (Min-Max)

(b) Mean power coefficient and power coefficient range (Min-Max)

**Fig. 12.** (a) Thrust coefficient and (b) power coefficient: mean values with min-max ranges versus submergence depth.

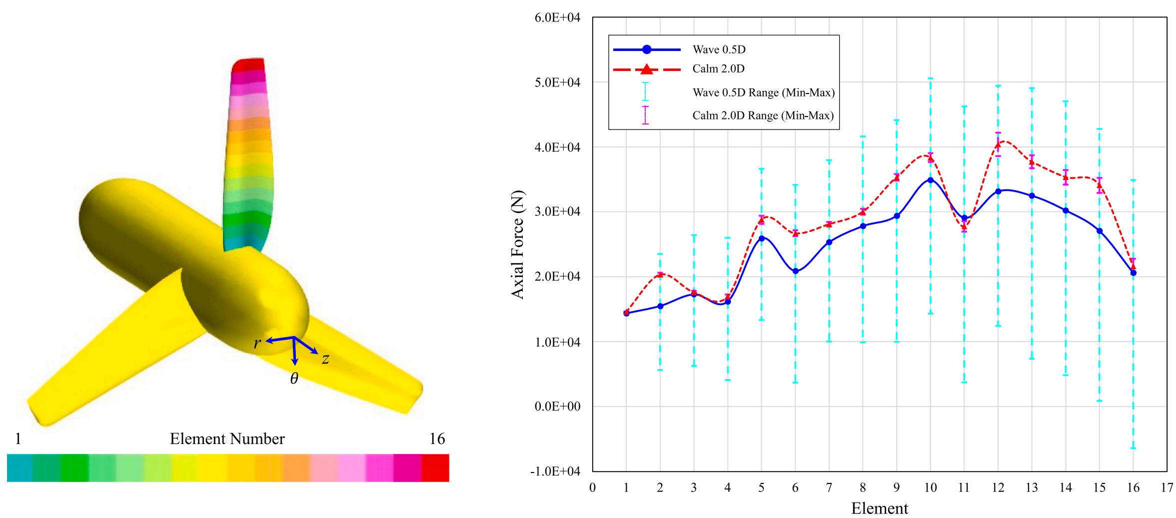


(a) Blade segmentation into 16 spanwise elements

(b) Mean axial force and axial force range (Min-Max)

**Fig. 13.** Blade load analysis. (a) Division of a single blade into 16 spanwise elements. (b) Mean axial force and fluctuation range (min-max) for each element under wave and calm conditions.

**Table 6**
Torque Statistics at different submergence depths.

| Case | Average (N·m) | Max (N·m) | Min (N·m) | Standard Deviation (%) |
|---|---|---|---|---|
| Wave 0.5D | 2.07E+06 | 3.96E+06 | 6.64E+05 | 55.16 |
| Wave 1.0D | 1.95E+06 | 2.60E+06 | 1.36E+06 | 22.08 |
| Wave 1.5D | 1.91E+06 | 2.16E+06 | 1.66E+06 | 8.85 |
| Wave 2.0D | 1.89E+06 | 2.00E+06 | 1.79E+06 | 3.52 |

submergence depth and generator efficiency. As submergence depth decreases and wave-induced torque fluctuations intensify, the estimated generator efficiency declines progressively, from 0.898 at Wave 2.0D to 0.896 at Wave 1.5D, 0.890 at Wave 1.0D, and 0.854 at Wave 0.5D. The most pronounced degradation occurs at the shallowest configuration, where the efficiency penalty relative to the baseline reaches 4.6 percentage points.

**Table 7**
Thrust coefficient ($C_T$) Statistics at different submergence depths.

| Case | Average | Max | Min | Standard Deviation (%) |
|---|---|---|---|---|
| Wave 0.5D | 0.854 | 1.304 | 0.456 | 29.64 |
| Wave 1.0D | 0.866 | 1.032 | 0.707 | 11.21 |
| Wave 1.5D | 0.860 | 0.928 | 0.796 | 4.45 |
| Wave 2.0D | 0.857 | 0.886 | 0.830 | 1.76 |

**Table 8**
Power coefficient ($C_P$) Statistics at different submergence depths.

| Case | Average | Max | Min | Standard Deviation (%) |
|---|---|---|---|---|
| Wave 0.5D | 0.516 | 0.987 | 0.165 | 28.49 |
| Wave 1.0D | 0.486 | 0.649 | 0.339 | 10.72 |
| Wave 1.5D | 0.476 | 0.539 | 0.415 | 4.21 |
| Wave 2.0D | 0.472 | 0.499 | 0.446 | 1.66 |

**Table 9**
Estimated generator efficiency based on copper loss analysis.

| | Wave 0.5D | Wave 1.0D | Wave 1.5D | Wave 2.0D | Calm 2.0D |
|---|---|---|---|---|---|
| $P_{in}$ (W) | 2.65E+06 | 2.49E+06 | 2.44E+06 | 2.42E+06 | 2.37E+06 |
| $P_{cu}$ (W) | 3.86E+05 | 2.75E+05 | 2.53E+05 | 2.48E+05 | 2.37E+05 |
| $P_{out}$ (W) | 2.27E+06 | 2.22E+06 | 2.19E+06 | 2.18E+06 | 2.14E+06 |
| Generator Efficiency | 0.854 | 0.890 | 0.896 | 0.898 | 0.900 |

This deterioration is directly attributable to the elevation of RMS torque caused by the increased standard deviation of torque fluctuations at shallow submergence depths, as reported in Table 6. The copper loss in the Wave 0.5D case reaches 3.86E+5W, representing an increase of approximately 63% relative to the Calm 2.0D baseline value of 2.37E+5W. In contrast, the Wave 2.0D case exhibits copper losses only marginally above the baseline, consistent with the attenuation of wave-induced orbital velocities at greater depth.

These findings suggest that the selection of installation depth involves a trade-off that extends beyond hydrodynamic performance alone. While shallower submergence may offer modest gains in mean power output due to enhanced wave-induced inflow velocities, the associated increase in torque variability imposes a measurable penalty on generator efficiency through elevated copper losses. This effect is expected to become increasingly significant under more energetic sea states or at sites with pronounced swell conditions.

It should be noted, however, that the present analysis is subject to several simplifying assumptions that limit its applicability as a precise engineering prediction. The baseline efficiency of $\eta_0 = 0.90$ is adopted as a representative value for direct-drive PMSGs and does not reflect the characteristics of any specific generator design. Furthermore, the analysis considers only copper losses and does not incorporate iron losses, mechanical friction losses, or power electronic converter losses, all of which contribute to the total loss budget of a real generator system. The absolute efficiency values reported in Table 9 should therefore be interpreted as indicative estimates intended to demonstrate the directional effect of torque variability on generator performance, rather than as quantitatively precise predictions. A comprehensive assessment of generator efficiency under wave conditions would require detailed electromagnetic modelling of the specific machine, which implies that the influence of waves on tidal turbine power output estimation warrants further dedicated investigation.

### *4.3. Section force acting on a single blade*

The wave-induced orbital velocity decays exponentially with distance from the free surface. This implies that at any given instant, the three blades of a tidal turbine each experience a distinct flow field. This phenomenon gives rise to a non-uniform load distribution across individual blades and the rotor as a whole, while simultaneously generating periodic axial load fluctuations. Consequently, the blades and blade roots of a tidal turbine operating under wave conditions are subjected to far more severe cyclic loading than those operating in still water, which may accelerate structural fatigue damage.

To quantitatively assess this effect, a single blade was divided into 16 spanwise elements and the axial force acting on each element was evaluated. A direct comparison was made between the Calm 2.0D baseline case, representing still-water conditions, and the Wave 0.5D case, which is subject to the most pronounced wave-induced effects. Fig. 13 presents the time-averaged axial force at each element for both cases, with the wave condition shown as a blue solid line and the calm condition as a red dashed line, along with min-max bars indicating the maximum and minimum values experienced at each element. The pressure fluctuations induced by wave loading are further illustrated in the supplementary video material (Video S1), which provides a visual representation of the unsteady pressure field evolution.

Supplementary data related to this article can be found online at https://doi.org/10.1016/j.oceaneng.2026.126189

Examining the mean axial force distribution, both cases exhibit a progressive increase from the blade root region (Element 1) towards the mid-span, reaching a peak at approximately Element 10, beyond which the load decreases towards the blade tip. Notably, the Calm 2.0D case yields consistently higher mean axial forces than the Wave 0.5D case across the entire span. This is attributed to the reduction in effective wetted blade area that occurs when a portion of the blade is intermittently exposed to air during wave trough passages.

In contrast, the fluctuation range reveals a striking difference between the two cases. The min-max bars for Calm 2.0D remain narrow throughout the entire span, indicating that the axial loads under still-water conditions are nearly invariant in time. Those for Wave 0.5D, however, are markedly wider at every element, with particularly large fluctuation ranges observed in the outer span region spanning Elements 9 to 16.

These results clearly demonstrate that the presence of waves fundamentally alters the nature of the loading experienced by the blade. In particular, the cyclic loading in the outer span region constitutes a far more severe fatigue condition than would be anticipated from design load cases based on still-water operation, suggesting that structural damage may occur well before the service life predicted by static strength criteria. It is therefore evident that the structural design of tidal turbines intended for wave-affected environments must account not only for mean loads but also for the amplitude of load fluctuations.

## 5. Conclusions

This study presents a systematic CFD-based analysis of the hydrodynamic behaviour of a full-scale horizontal-axis tidal turbine operating under combined wave-current conditions at four submergence depths (0.5D, 1.0D, 1.5D, and 2.0D). By quantifying the wave-induced effects on torque, thrust coefficient, power coefficient, generator copper losses, and individual blade loading, the following conclusions are drawn.

Wave-induced torque fluctuations increase sharply as submergence depth decreases, consistent with the exponential attenuation of wave orbital velocity with depth. At the shallowest condition, Wave 0.5D, the torque varies from −68% to +91% of the mean value, yielding a peak-to-trough fluctuation range of approximately 159%. In contrast, at Wave 2.0D, the fluctuation remains within ±6% of the mean, approaching the steady-state behaviour observed under still-water conditions.

Regarding mean performance coefficients, the power coefficient ($C_P$) increases monotonically as the rotor approaches the free surface, rising from 0.472 at Wave 2.0D to 0.516 at Wave 0.5D, attributable to the enhancement of wave-induced inflow velocity near the free surface. The thrust coefficient ($C_T$), by contrast, exhibits non-monotonic behaviour, reaching a maximum of 0.866 at Wave 1.0D before declining to 0.854 at Wave 0.5D. This reduction at the shallowest depth is attributed to the intermittent exposure of the blade tips to air during wave trough passages, which reduces the effective swept area. The standard deviations of both coefficients increase sharply with decreasing submergence depth, reaching 29.64% and 28.49% for $C_T$ and $C_P$ respectively at Wave 0.5D, compared to only 1.76% and 1.66% at Wave 2.0D.

A simplified copper loss analysis based on RMS torque reveals that wave-induced torque variability imposes a significant penalty on generator efficiency. Adopting a baseline efficiency of $\eta_0 = 0.90$ for the still-water reference case, the estimated generator efficiency decreases progressively with decreasing submergence depth, reaching 0.854 at Wave 0.5D, a reduction of 4.6 percentage points relative to the baseline. The copper losses at the shallowest condition increase by approximately 63% relative to the still-water baseline, highlighting the necessity of accounting for electromagnetic losses in the generator when assessing the net energy yield of tidal turbines deployed in wave-affected environments.

Spanwise blade load analysis confirms that wave conditions fundamentally alter the nature of the loading experienced by individual blades. Calm 2.0D maintains a narrow load fluctuation range across the entire span, whereas the Wave 0.5D exhibits markedly wider fluctuation ranges, particularly in the outer span region spanning Elements 9 to 16. Although the mean axial force is higher under still-water conditions due to the absence of blade air exposure, the amplitude of cyclic loading under wave conditions is substantially greater, creating a fatigue environment far more severe than would be anticipated from design load cases based on still-water operation.

In summary, the findings of this study demonstrate that the selection of installation depth involves complex trade-offs that extend well beyond mean hydrodynamic performance. While shallower submergence offers modest gains in mean power output through enhanced wave-induced inflow velocities, the accompanying increase in load variability imposes substantial penalties on both structural fatigue life and generator efficiency. The results provide quantitative engineering guidance for optimizing turbine installation depth at wave-active tidal energy sites, and underscore the necessity of incorporating wave-induced unsteady loading into both the structural design and energy yield assessment frameworks for tidal turbines.

## CRediT authorship contribution statement

**Kangmin Kim:** Writing – original draft, Investigation, Formal analysis, Data curation. **Gyeongseo Min:** Writing – review & editing. **Haechan Yun:** Writing – review & editing. **Younguk Do:** Writing – review & editing. **KeoungHyun Jung:** Writing – review & editing. **Weichao Shi:** Writing – review & editing, Supervision. **Daejeong Kim:** Writing – review & editing, Supervision. **Soonseok Song:** Writing – review & editing, Supervision, Methodology, Investigation, Funding acquisition.

## Declaration of competing interest

The authors declare that they have no known competing financial interests or personal relationships that could have appeared to influence the work reported in this paper.

## Acknowledgements

The research presented in this study was supported by the KAIA Research program on the Development of Marine Bridges Operation using Green Energy, funded by the Ministry of Land, Infrastructure and Transport [Grant number: RS-2024-00401101].

## Appendix A. Supplementary data

Supplementary data related to this article can be found at https://doi.org/10.1016/j.oceaneng.2026.126189.

## References

Ahmed, U., Apsley, D., Afgan, I., Stallard, T., Stansby, P., 2017. Fluctuating loads on a tidal turbine due to velocity shear and turbulence: comparison of CFD with field data. Renew. Energy 112, 235–246.

Allsop, S., Peyrard, C., Thies, P.R., Boulougouris, E., Harrison, G.P., 2017. Hydrodynamic analysis of a ducted, open centre tidal stream turbine using blade element momentum theory. Ocean. Eng. 141, 531–542.

Apsley, D.D., Stallard, T., Stansby, P.K., 2018. Actuator-line CFD modelling of tidal-stream turbines in arrays. Journal of Ocean Engineering and Marine Energy 4 (4), 259–271.

Bahaj, A.S., Batten, W.M.J., McCann, G., 2007a. Experimental verifications of numerical predictions for the hydrodynamic performance of horizontal axis marine current turbines. Renew. Energy 32 (15), 2479–2490. https://doi.org/10.1016/j.renene.2007.10.001.

Bahaj, A.S., Molland, A.F., Chaplin, J.R., Batten, W.M.J., 2007b. Power and thrust measurements of marine current turbines under various hydrodynamic flow conditions in a cavitation tunnel and a towing tank. Renew. Energy 32 (3), 407–426. https://doi.org/10.1016/j.renene.2006.01.012.

Batten, W.M.J., Bahaj, A.S., Molland, A.F., Chaplin, J.R., 2008. The prediction of the hydrodynamic performance of marine current turbines. Renew. Energy 33 (5), 1085–1096. https://doi.org/10.1016/j.renene.2007.05.043.

Celik, I.B., Ghia, U., Roache, P.J., 2008. Procedure for estimation and reporting of uncertainty due to discretization in CFD applications. Journal of fluids Engineering-Transactions of the ASME 130 (7). https://doi.org/10.1115/1.2960953兴.

Chapman, S.J., 2003. Electric Machinery Fundamentals, vol. 5. McGraw-Hill Education.

El-Shahat, S.A., Li, G., Fu, L., 2021. Investigation of wave–current interaction for a tidal current turbine. Energy 227, 120377.

Fenton, J.D., 1985. A fifth-order stokes theory for steady waves. J. Waterw. Port, Coast. Ocean Eng. 111 (2), 216–234.

Ferziger, J.H., Perić, M., Street, R.L., 2002. Computational Methods for Fluid Dynamics, vol. 3. Springer.

Gaurier, B., Davies, P., Deuff, A., Germain, G., 2013. Flume tank characterization of marine current turbine blade behaviour under current and wave loading. Renew. Energy 59, 1–12.

Guy, C., Hart, E., Vengatesan, V., Forehand, D., 2024. Numerical modelling of a 1.5 MW tidal turbine in realistic coupled wave–current sea states for the assessment of turbine hub-depth impacts on mechanical loads. Ocean. Eng. 292. https://doi.org/10.1016/j.oceaneng.2023.116577.

Ittc, R., 2011. Procedures and Guidelines: Practical Guidelines for Ship CFD Applications, 7.5. ITTC, Boulder, CO, USA.

Lewis, M.J., Neill, S.P., Hashemi, M.R., Reza, M., 2014. Realistic wave conditions and their influence on quantifying the tidal stream energy resource. Appl. Energy 136, 495–508. https://doi.org/10.1016/j.apenergy.2014.09.061.

Martinez, R., Payne, G.S., Bruce, T., 2018. The effects of oblique waves and currents on the loadings and performance of tidal turbines. Ocean. Eng. 164, 55–64. https://doi.org/10.1016/j.oceaneng.2018.05.057.

Masters, I., Chapman, J., Willis, M., Orme, J., 2011. A robust blade element momentum theory model for tidal stream turbines including tip and hub loss corrections. Journal of Marine Engineering & Technology 10 (1), 25–35.

MeyGen Ltd, 2019. Meygen Tidal Energy Project: Phase 1A Operational Report. Technical Report. MeyGen Ltd., UK.

Min, G., Choi, W., Yun, H., Do, Y., Kim, K., Shi, W., Dai, S., Kim, D., Song, S., 2025. Evaluation of free-surface exposure effects on tidal turbine performance using CFD. J. Mar. Sci. Eng. 13 (8), 1589.

Orbital Marine Power, 2022. O2 Tidal Turbine: Technical Specification. Technical Report. Orbital Marine Power Ltd., UK.

Perez, L., Cossu, R., Grinham, A., Penesis, I., 2022. Tidal turbine performance and loads for various hub heights and wave conditions using high-frequency field measurements and blade element momentum theory. Renew. Energy 200, 1548–1560. https://doi.org/10.1016/j.renene.2022.10.058.

Shi, W., Rosli, R., Atlar, M., Norman, R., Wang, D., Yang, W., 2016. Hydrodynamic performance evaluation of a tidal turbine with leading-edge tubercles. Ocean. Eng. 117, 246–253. https://doi.org/10.1016/j.oceaneng.2016.03.044.

Si, X., Xie, Y., Tan, J., Yuan, P., Wang, S., Liu, Y., Liu, X., 2024. Study on the impact of wave characteristics on the performance of full-scale tidal turbine. Ocean. Eng. 303. https://doi.org/10.1016/j.oceaneng.2024.117800.